

Calibration of colour gradient bias in shear measurement using CANDELS

X. Er¹*, H. Hoekstra², T. Schrabback³, V. F. Cardone¹, R. Scaramella¹, R. Maoli⁴, M. Vicinanza^{1,4,5}, Bryan Gillis⁶ L. Miller⁷, J. Rhodes^{8,9}

¹ I.N.A.F. - Osservatorio Astronomico di Roma, via Frascati 33, 00040 - Monte Porzio Catone, Roma, Italy

² Leiden Observatory, Leiden University, PO Box 9513, NL-230 RA, Leiden, the Netherlands

³ Argelander Institute fuer Astronomie, Auf dem Huegel 71, D-53121 Bonn, Germany

⁴ Dipartimento di Fisica, Universita di Roma "La Sapienza", Piazzale Aldo Moro, 00185 - Roma, Italy

⁵ Dipartimento di Fisica, Universita di Roma "Tor Vergata", via della Ricerca Scientifica 1, 00133 - Roma, Italy

⁶ Royal Observatory, University of Edinburgh, Blackford Hill, Edinburgh EH9 3HJ, UK

⁷ Department of Physics, Oxford University, keble Road, Oxford OX1 3RH, UK

⁸ Jet Propulsor Laboratory, California institute of Technology, 4800 Oak Grove Drive, Pasadena, CA 91109, USA

⁹ California Institute of Technology, 1200 East California Blvd, Pasadena, CA 91125, USA

Accepted –; received –; in original from 9 January 2017

ABSTRACT

In weak gravitational lensing, the precision strongly depends on the shape measurement of the galaxy images. Observation using wide band filter can provide images with high signal-to-noise ratio, and can cover a large redshift range as well. However, the shape measurement requires analysis of the point spread function (PSF). In general, both the PSF and the galaxy are chromatic, i.e. the shapes vary with wavelength. Thus, measuring the shape of galaxies using integrated images over the filter will cause higher order systematic bias, which is called colour gradient bias. We perform an estimate of this bias using both simulated images and real data from CANDELS. We show that the estimation for colour gradient bias using two narrow bands can reach a high precision in the simulated noisy data. The estimation using noisy images has a large scatter, which may over-estimate the magnitude of the bias. In our sample of real galaxy images, we find correlations between the bias with the colour and the size of the galaxy. Moreover, we find that the higher order image distortions, such as flexion, will enlarge the colour gradient bias in shear, although it affects the estimation only when the images are in strong lensing regions.

Key words: cosmology, weak lensing, systematics

1 INTRODUCTION

Weak gravitational lensing has been identified as a powerful method in cosmology, such as mapping the large scale structures. The images of distant galaxy are distorted by the gravitational potential generated by the intervening matter. A statistical analysis of image distortion of background galaxies provides crucial information about the mass distribution and thus tight constraint to the cosmological models (e.g. Bartelmann & Schneider 2001; Hoekstra & Jain 2008).

The precision of measuring the shapes of the galaxy images is limited due to the atmospheric turbulence, i.e. Point Spread Function (PSF). Thus space telescopes can take the advantage of small space PSF, e.g. the future weak lensing survey loaded on the Euclid satellite. The weak lensing survey by Euclid plans to provide a large sample of accurate measurements of both shape and photo-

tometric redshift for the galaxies. The filter of the Euclid image survey has a very wide bandpass (550nm – 920nm), which covers a large range of redshift of galaxies and can also obtain galaxy images with high signal-to-noise ratio (SNR).

In shear measurements, the galaxy shape is corrected using the effective (integrated) PSF. However, the galaxies in general have different intrinsic shapes at different wavelengths, as well as the PSF, e.g. the size of PSF is slightly larger at longer wavelength. (Meyers & Burchat 2015) have also shown that the differential chromatic refraction can introduce systematics to the measurement of galaxy shapes. The chromatic PSF causes a bias in the measurement, which can be estimated and reduced to the required levels using a colour weighted PSF (Cypriano et al. 2010). While the correction described in Cypriano et al. (2010) assumes a uniform spectral energy distribution (SED) of the source galaxy. It becomes inaccurate when the SED, or colour of the source galaxy varies spatially. The effects introduce a higher order systematic bias in measuring the shape of galaxies, if one uses the integrated im-

* er.xinzhong@oa-roma.inaf.it

ages and integrated PSF. The bias, which we called colour gradient (hereafter CG) bias, has dependence on several factors: such as the SED of the galaxy, the relative size of the galaxy to the PSF, as well as the bandwidth of the filter. The relative magnitude of the CG can be neglected for narrow band survey. However, the CG bias is expected to be relevant for Euclid, especially since the error budget of Euclid weak lensing project is small (e.g. Cropper et al. 2013; Massey et al. 2013).

In (Voigt et al. 2012; Sembolini et al. 2013), the simulated images with Euclid features are used to study the CG bias. A potential bias of level 10^{-3} is found for typical size galaxies even with a smooth SED, i.e. without strong emission or absorption lines. Moreover, it has been shown that using two high resolution narrow band, noise free images, one can calibrate the CG bias with high precision for a specific subset of galaxies, e.g. the galaxies without strong emission/absorption lines. In this work, we will demonstrate the result and the method in Sembolini et al. (2013)(ES13 in the rest of this paper), and apply the calibration method to the simulated noisy images. The method requires that the match of the bandwidth. Fortunately, the bandwidth of weak lensing survey on Euclid can be cover by two filters on the Hubble Space Telescope (HST), i.e., F606W and F814W.

The colour gradients in the galaxy have been widely studied. It has been found that the negative colour gradients (redder in the centre and bluer in the outskirts) exist in the elliptical galaxies, and steeper colour gradients are more commonly found in bluer or more luminous early type galaxy (e.g. den Brok et al. 2011; Gonzalez-Perez et al. 2011). La Barbera et al. (2010); Kennedy et al. (2016) also suggest correlations between colour gradients and the overall colour and luminosity of the galaxies. The formation of galaxy, e.g. inside-out growth through gas accretion or major mergers, will cause distinct morphologies as well as colour gradients (e.g. Tortora et al. 2010). Therefore, one expect that the CG bias has dependence on such factors.

In Section 2, we will introduce the basic concept of gravitational lensing and CG bias. The simulated images are presented to study the bias, following the similar method in ES13. In Section 4 we will apply the calibration method to a galaxy sample selected from HST CANDELS data (Schrabback et al. in prep.) and give our discussion and conclusion in the end.

2 BASIC FORMULISM

We introduce the basic symbols and parameters that will be used in this paper. We use angular coordinate θ on the lens plane, and $\gamma = \gamma_1 + i\gamma_2$ is the complex lensing shear. We consider an image of a galaxy, and denote the photon brightness distribution of the image at each wavelength λ by $I(\theta, \lambda)$, which is related to the intensity $S(\theta, \lambda)$ by $I(\theta, \lambda) = \lambda S(\theta, \lambda)$. Due to the PSF $P(\theta, \lambda)$ and filter of the telescope $F(\lambda)$, the image of a galaxy observed with a filter of width $\Delta\lambda$ is given by

$$I^{obs}(\theta) = \int_{\Delta\lambda} I(\theta, \lambda) * P(\theta, \lambda) F(\lambda) d\lambda, \quad (1)$$

where $*$ denotes a convolution. In the weak lensing regime, the shear can be estimated from the ellipticity of the source galaxy, which is usually a measurement of second order brightness moments Q_{ij} (Bartelmann & Schneider 2001)

$$e_1 + ie_2 \approx \frac{Q_{11} - Q_{22} + 2iQ_{12}}{Q_{11} + Q_{22} + 2(Q_{11}Q_{22} - Q_{12}^2)^{1/2}}, \quad (2)$$

where the second order brightness moments are given by

$$Q_{ij} = \frac{1}{S_0} \int I^{obs}(\theta) \theta_i \theta_j W(\theta) d^2\theta \quad (i, j = 1, 2), \quad (3)$$

where $S_0 = \int d^2\theta W(\theta) I^{obs}(\theta)$ is the total observed brightness, and $W(\theta)$ is the weight function. The moment-based methods, such as KSB (Kaiser et al. 1995) or DEIMOS (Melchior et al. 2011) will be biased due to the weight function, which causes dependence of the CG bias to the properties of weight function. In this paper, we will limit the method to the brightness moments, and use the circular Gaussian weighting function with the size of half light radius.

The CG bias is estimated from following steps (see ES13 for more details): we first generate the image in each wavelength from the galaxy model. Then we shear the images, and apply the convolution with PSF before integrating over the wavelength. Since both the galaxy and the PSF are chromatic, the integrated image contains CG bias. We also need the flat SED image, which contains non-colour gradient (NCG), and is the ideal image for shear measurement. The NCG images can be generated by

$$I^{NCG}(k, \lambda_{ref}) = \frac{F(\lambda_{ref}) I^{obs}(k)}{P_{eff}}, \quad (4)$$

where $I^{obs}(k)$ is the galaxy image (Eq.1) in Fourier space. The deconvolution is performed with the effective PSF

$$P_{eff}(\theta) = \int d\lambda P(\theta, \lambda) F(\lambda), \quad (5)$$

which is the PSF integrated over the filer band. The NCG images are the uniform image over the wavelength. One can see Fig.1 for the steps of generating the CG and NCG images. We need to emphasize here that the images we generated to estimate the CG bias are independent of the measurement method. As we will shown in the appendix, in the moment method, if we convolve the two images with the same PSF, the ratio of the ellipticity from two images does not change. Comparing the ellipticity (shear) measured from the two images we will have the multiplicative CG bias (Heymans et al. 2006)

$$m = \frac{e_i^{CG}}{e_i^{NCG}} - 1, \quad (6)$$

where e_i refers to the measurement of the first or second component of the ellipticity. In principle, the two components e_1 or e_2 will give the same estimation of the CG bias. Due to the intrinsic shape of the galaxy images, the two components may have a different response, which can be avoided by rotating the galaxy images. In this work, we will use one ellipticity component $e_1^{CG}/e_1^{NCG} - 1$ as our estimate if not specified. The additive bias can be detected by correlating the estimated shear and will not be considered here.

3 COLOUR GRADIENT BIAS IN SIMULATED DATA

The CG bias is a higher order systematic bias, the numerical noise in simulated images may cause extra error in our analysis. Thus, we first adopt two independent codes to generate the simulated images: one is C/C++ and the other is python-based GalSim package (Rowe et al. 2015). In the C code, we directly calculate the brightness density at the centre of each pixel, and sample the image using the approximate brightness in each pixel (brightness at the centre multiply the area of pixel). In GalSim the image are sampled by

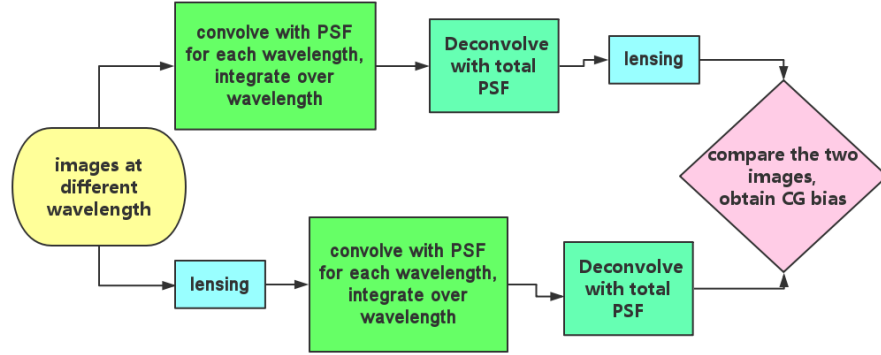


Figure 1. The steps of how we simulated CG (bottom flow) and NCG (top flow) images to estimate the shear CG bias.

FFT rendering. The circular images are used for the source galaxy. We check the initial mock image, especially the convolution and deconvolution step. No significant ellipticity are found in neither C or GalSim. Since the deconvolution is particularly difficult in the numerical calculation, we also perform that for the elliptical images. A small relative error $\sim 10^{-6}$ appear in ellipticity using both C and GalSim, which is two orders of magnitude smaller than the possible CG bias.

We apply the two same galaxy models as in ES13. It will allow us to further check the numerical error, since in ES13 the images are simulated by different code. The images are consist of two components: bulge and disk, both are modeled by a Sersic profile with index n

$$I_{\text{Sersic}}(\theta) = I_0 e^{-\kappa \theta^{1/n}}, \quad (7)$$

where I_0 is the central intensity, and $\kappa = 1.9992 n - 0.3271$. For the SED of the bulge and the disk we use the galaxy templates from Coleman et al. (1980). The SED of the bulge is modeled by an elliptical galaxy, and SED of irregular galaxy for the disk. We choose an extremely blue SED for disk to generate large colour gradient in the galaxy images. For each wavelength, we construct the galaxy image $I(\theta, \lambda)$ by adding up the profiles of bulge and disk normalised by fixing the ratio $S_{\text{bulge}}/S_{\text{disk}}$ at $\lambda = 550\text{nm}$. The integrated profile is applied to the Euclid filter in a wavelength range [550 : 920]nm with a step of 1nm. The images are constructed in an isolated stamp with size 256×256 pixels, and resolution 0.05 arcsec/pixel (Table 2).

We use different reference PSF models. The first one is a Gaussian profile, with wavelength dependent width:

$$\sigma_{\text{psf}}(\lambda) = w_{0,800} \left(\frac{\lambda}{800\text{nm}} \right), \quad (8)$$

where $w_{0,800}$ is the width of the PSF at 800nm. In this section we use $w_{0,800} = 0.102$ arcsec, which is the same as in ES13. The other reference model is an Airy function, which is close to the Design profile (Laureijs et al. 2011)

$$P(\theta) = \frac{I_0}{(1-\epsilon^2)^2} \left(\frac{2J_1(x)}{x} - \frac{2\epsilon J_1(\epsilon x)}{x} \right)^2, \quad (9)$$

where I_0 is the maximum intensity at the center, ϵ is the aperture obscuration ratio, and $J_1(x)$ is the first kind of Bessel function of order one. x is defined as $x = \pi\theta/l$, where $l = \lambda/D$ is wavelength over diameter ($\epsilon = 1/3$, $D = 1.2$ for Euclid). In Fig. 2, we compare the Airy model with other PSF models.

PSF	Description
Gaussian	Gaussian PSF described by Eq. 8 with $w_{0,800} = 0.102$
GaussianT	Gaussian core described by Eq. 8 with $w_{0,800} = 0.054$ plus top-hat with 20 percent of the total flux the cut-off size $\propto \lambda^{0.74}$ (ES13)
Airy	Airy model with obscuration 1/3 (Eq.9)

Table 1. The PSF models shown in Fig. 2. The Gaussian model, which is the same PSF model in ES13 is used for the simulated images. The GaussianT model is a Gaussian core plus a top hat function (ES13), which is shown as a comparison with Airy model. The Airy model is used for the bias calibration and HST data analysis in the following section.

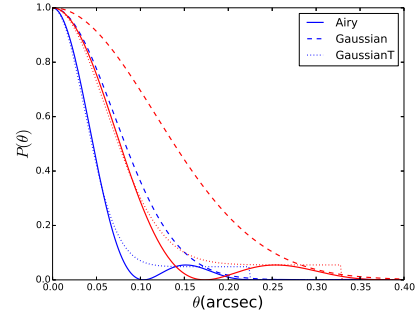


Figure 2. Comparison of the PSF models at 550nm (blue) and 920nm (red); the solid, dashed and dotted lines are the Airy, Gaussian and GaussianT PSF models respectively (Table 1).

We measure the CG bias as a function of weight size (Fig.3). The solid lines are the results from ES13, and the dashed (dotted) lines are the results using C (GalSim) code. The blue and green lines are the CG bias of small size galaxy (S-galaxy), while the red and purple lines are that of big size galaxy (B-galaxy). One can see that the CG bias from all three different simulated galaxies are

Name	SED	axis(arcsec)	flux ratio (550nm)	Sersic index n
B-galaxy	E/Irr	0.17/1.2	1:3	1.5/1.0
S-galaxy	E/Irr	0.09/0.6	1:3	1.5/1.0

Table 2. Parameters of simulated galaxies: when two values are quoted in a column, the first refers to the bulge, the second to the disc.

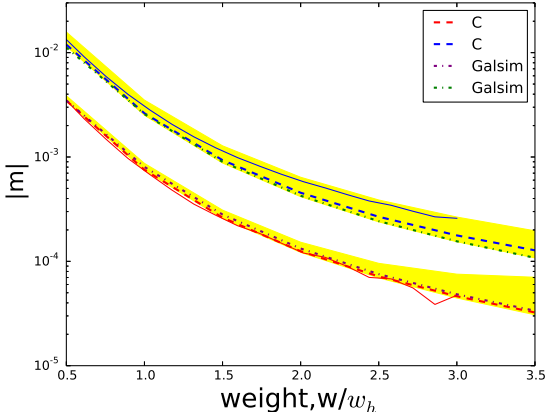


Figure 3. The CG bias in shear versus weight function. The solid lines are the results from paper ES13. The dashed (dash-dotted) lines are the results of this work using images simulated from C (GalSim) code. The blue (red) lines are the result for small (big) size simulated galaxies. The yellow shadow is the variation introduced by higher order image distortions. w_h is half light radius of the galaxy image.

consistent, i.e. the numerical error does not introduce significant bias in this study. Thus, in the following of this section, we will only use the GalSim to generate the mock galaxies. The CG bias decreases with the increasing weight size. As the optimal choice to maximize the signal-to-noise ratio is to match the weight function to the size of the source galaxy, we will use the half light radius for the weight function in the following of this paper. For the two mock galaxies, the CG bias with such a weight function is 0.8×10^{-3} , 2×10^{-3} for B- and S-galaxy respectively. The smaller size galaxies have a larger CG bias, which suggests that the calibration of the CG bias need to take into account of the size as well as the real colour gradient of the galaxy.

Besides shear, there are higher order image distortions in weak lensing, such as flexion (e.g. Goldberg & Natarajan 2002; Bacon et al. 2006). In previous analysis, we only consider the shear effect in the lensing process, while the higher order image distortions also suffer from CG bias as well. In additional tests, we perform the complete lens ray-tracing instead of solely shearing the images. (We only use our C code in this part, since the current version of GalSim only provides shear effect.) We adopt an Singular Isothermal Sphere halo model as the lens model, and vary the configuration within some reasonable range, such as the Einstein radius, and the separation between the lens and the source image (the corresponding shear value varies between about [0.02, 0.1]). We find that the variation of lensing magnitude can cause different CG bias (yellow shadow in Fig.3), and in most time the flexion effect will increase the CG bias. Such effects do not appear if we solely shear the images. However in general case, the cosmic shear has a value about a few percents. We can see that from the bottom boundary of the yellow shadow, the bias are almost the same as that only considering the shear effect. Only in case of the galaxy cluster lensing, galaxy-galaxy lensing, especially in the strong lensing region, when the flexion becomes significant, one has to take into account of such kind of effect.

3.1 Calibration of CG bias using simulated HST images

We outline the method that calibrate the CG bias using two bands images, while the details can be found in ES13. We will use two narrow band images to reconstruct the image at each wavelength. For each of the narrow filter the image can be approximated by:

$$I_i(\theta) = \int_{\Delta\lambda_i} T_i(\lambda) I(\theta, \lambda) d\lambda, \quad (10)$$

where $T(\lambda)$ is the transmission, and $i = 1, 2$ stand for the two bands. We assume that for each pixel the image can be interpolated linearly:

$$I(\theta, \lambda) \approx I_{\text{inter}}(\theta, \lambda) = a(\theta)\lambda + b(\theta). \quad (11)$$

Eqs.10 and 11 yield a linear set of equations on each pixel, which can be used to solved for the coefficients (a, b) :

$$T_{ai}\lambda a(\theta) + T_{bi}b(\theta) = I_i(\theta), \quad i = 1, 2, \quad (12)$$

where $T_{ai, bi}$ is the integrated transmission function at two filters. With (a, b) and Eq.11, one can obtain approximated galaxy images of each wavelength $I(\theta, \lambda)$. Then we will follow the same procedure as in previous section to estimate the CG bias.

The same two galaxy models from previous section are used in the simulation, and we simulate the images in two HST filters: F606W, F814W, which cover the filter of Euclid image survey. The spectra of the galaxy are shifted according to their redshift, but the evolution of the galaxy or the cosmology are not adopted in the simulation. The spatial resolution is 0.05 arcsec/pixel. The PSF is modeled by the Airy function with diameter $D = 2.5$ and obscuration 0.33, which is the configuration of HST. As shown in ES13, one needs to correct the PSF effect in the observed images, or the CG bias will be underestimated. We will adopt the same step: deconvolution for images before the bias estimation and discuss that for the noisy images later.

In order to see the effect of noise in the galaxy image, we add Gaussian noise into the simulated HST images. An ideal level (SNR=50) and a moderate level (SNR=15) are used to see the effect of the CG bias. The RMS of the Gaussian image noise is determined by the total flux (F_{tot}) within a certain radius $1.5 r_h$

$$\sigma = \frac{F_{tot}}{\text{SNR} \sqrt{N_{tot}}}, \quad (13)$$

where N_{tot} is the total pixel number within $1.5 r_h$. In Fig.4, we compare the input SNR with that estimated by SExtractor (Bertin & Arnouts 1996). We can see that the estimations are slightly higher than the input values at $\text{SNR} = 15$, but still within a reasonable value for real weak lensing survey.

Direct devonvolution of a noisy image will end with a strange galaxy image and large numerical noise, thus we apply Galfit (Peng et al. 2010) to fit the noisy image, and use the fitted image as our noise reduced observed image, i.e. the residual noise is not taken into account for CG analysis. For the necessary fitting profile and number of components, we also use two Sersic components as bulge and disk for both image bands. For each image, we apply further constraints to the galaxy parameters: Sersic index, effective radius, and axis ratio (Table 3). We also compare with the input models, and find that the Sersic index is more difficult to fit than the effective radius.

In order to provide a initial parameters for Galfit, we use the stacked image of two bands to estimate the center and some initial values of the galaxy parameters from SExtractor. The fitting images slightly depend on the initial values, and can effect the estimate for

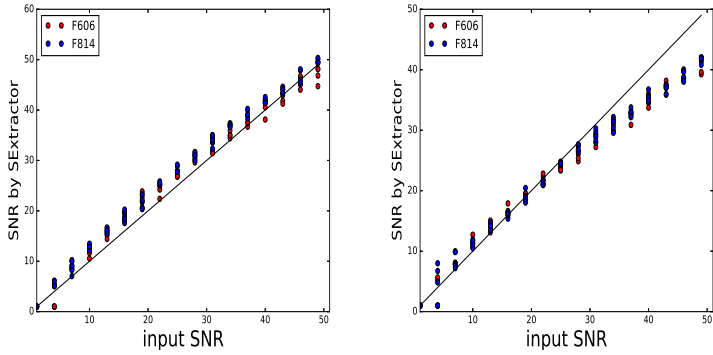


Figure 4. SNR estimated by SExtractor vs input SNR. Left is for the B-galaxy; Right is for the S-galaxy.

	S-606W	S-814W	B-606W	B-814W
n_1	0.5-2.5	0.5-2.5	0.5-2.5	0.5-2.5
n_2	0.5-2.5	0.5-2.5	0.5-2.5	0.5-2.5
R_{bulge}	1-10	1-10	3-30	3-30
R_{disk}	5-30	5-30	10-60	10-60
q	0.6-1	0.6-1	0.6-1	0.6-1

Table 3. Constraints for the fitting parameters in Galfit. The first two columns are for two images of the S-galaxy, the other two are the image of B-galaxy. n_1 is the Sersic index for bulge, and n_2 is the Sersic index for disk. The effect radius is given in unit of pixel (0.05 arcsec).

the CG bias estimation. The dependence will become significant with the decreasing of image SNR. In the following estimation for the CG bias, we will perform the image fitting using two kinds of initial parameters: in the first one we will leave all the fitting parameters free; while in the other one we will freeze the Sersic index as the simulated value, and leave the others free. As we will present, with sufficient large samples, the estimation using noisy images for the CG bias can converge, and is independent of the initial parameters.

Applying the calibration method to the fitted images, we can obtain the estimation of the CG bias for the simulated images. In Figs.5 and 6, we show the shear CG bias with redshift. In each panel, we show different estimates for the bias:

- The black solid lines are the “True” CG bias: we use the true SED of the galaxy and images of each wavelength to estimate the bias without approximation.
- The dashed lines are the estimation using two HST images without noise.
- The colour lines are those using noisy images. The difference between red and blue lines are in the step of Galfit: for the red lines, we free all the parameters in image fitting, for blue lines we fix the Sersic index as the input value. For the orange lines we also free all the parameters, but we perform another convolution with the effective PSF (see appendix for more detail). In Fig.1 one can see that the convolution is canceled with the last deconvolution for the CG images. The reason for that is the deconvolution may cause some numerical errors, especially for the small size noisy images. The extra PSF convolution will not significantly change the CG bias as we will show in the appendix. Therefore, in the following

result for noise images, we will perform the convolution to the NCG image instead of deconvolution to the CG one.

Moreover, although we use the circular source image in the simulation, the fitted noisy images will become slightly elliptical. In order to get rid of the error due to the “intrinsic shape”, we rotate the source image 6 times, and use the average value as our estimate for the galaxy ellipticity (Nakajima & Bernstein 2007). At each redshift, we use one noise free image and 40(200+) noisy images for $SNR = 50(SNR = 15)$. In the bottom panel of each figure, we also show the residues with respect to the true CG bias, and the error bars, which are given by the standard deviation from e_{cg} and e_{ncg}

$$\sigma_m = |m| \sqrt{\left(\frac{\sigma_{cg}}{\langle e_{cg} \rangle} \right)^2 + \left(\frac{\sigma_{ncg}}{\langle e_{ncg} \rangle} \right)^2}. \quad (14)$$

In the error panel, the grey shadow stands for the error budget of CG bias in Euclid cosmic shear analysis (± 0.00025 Cropper et al. 2013; Massey et al. 2013).

One can see that in general our estimate can reproduce the properties of CG bias in ellipticity measurement using both ideal or noisy images. In the high SNR cases (Fig.5), all the estimates with different initial parameters basically agree with each other, and reproduce the properties of the CG bias as a function of redshift. The estimate with all fitting parameters free gives lower bias than that fixed the Sersic index. In the realistic SNR case (Fig.6), the fitting using all free parameters show better estimates for the CG bias, and the errors are within the requirement for most cases. The variance due to the image fitting with different initial parameters are larger than high SNR cases, but can still be reduced by large sample of images and reach the requirement. Therefore, for each type of galaxy, at one redshift, we need at least 300 galaxy images for calibrating the bias. The scatters in the estimation are proportional to the magnitude of the bias, i.e. we have large uncertainty for S-galaxy at low redshift. In additional tests using other measurement methods for PSF correction, such as the image fitting methods (e.g. Miller et al. 2007; Kitching et al. 2008; Miller et al. 2013), and KSB+ (e.g. Hoekstra et al. 1998; Heymans et al. 2006), we find that the bias has similar dependence on the SED of the galaxies, although the magnitudes are different.

In all estimates, both low and high SNR, we notice that at $z = 0.5$ and 0.9 , the estimates are significantly smaller than the true value for both galaxy models. This is due to the uneven SED of the source galaxy in the two HST filter. In Fig.7, we compare the SED of the galaxy in redshift $z = 0, 0.5$. One can see that at $z = 0.5$, besides the strong emission lines, the linear approximation cannot reflect the properties of the source galaxies. Thus for the galaxies with strong emission lines, two wide band images are certainly not sufficient to calibrate the CG bias.

3.2 PSF variations in calibration data from HST

In the previous test, we used an ideal circular symmetric Airy PSF model. It may however cause inaccuracy in our estimation of the CG bias. Thus, we perform additional tests due to the variations of the PSF. The noise free images are used in order to isolate the effects of the PSF. The different PSF models are applied only in the step of deconvolution for the simulated HST images.

First we generate three pairs of PSF model by slightly increasing the size of PSF. The effect on the CG bias is shown in Fig.8. From solid, dashed to dotted lines, we increased the PSF size of the F606 bands; while from red, green to blue lines, we increase the

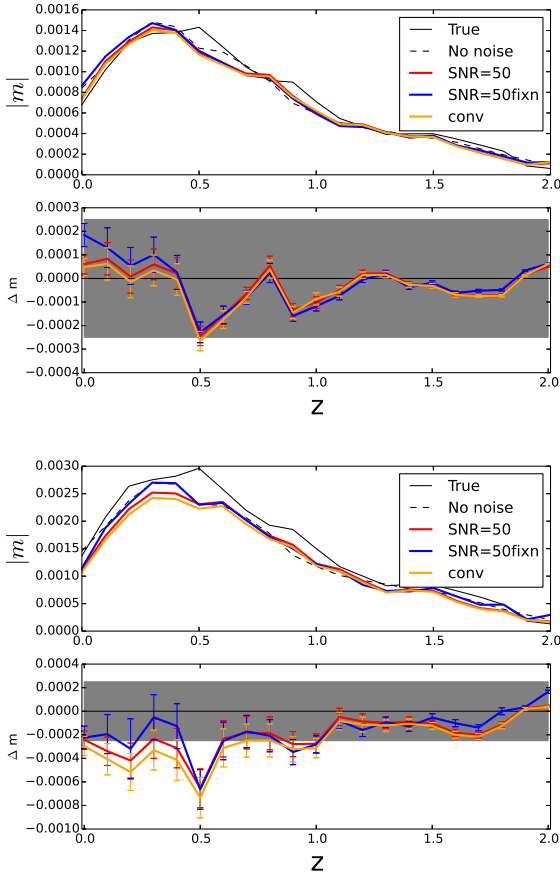


Figure 5. The CG bias in shear measurement as a function of redshift using simulated images. The black solid lines are the true CG bias; the dashed lines are the estimation using two band HST images without noise; the colour lines are the estimation using noisy images of input $SNR = 50$, the value are the average over 40 realizations each redshift. In the bottom, Δm is the residual with respect to the true CG bias, and the error bars show the standard variations (Eq.14). Up(Down)-figure are the results for B-(S-)galaxy.

PSF size of the F814 bands. Although the effect due to the two PSF variations depends on the SED of the source galaxy, one can see that increasing the size of the PSF in different bands will cause either an increase or decrease in the CG bias calibration. Once again, we can see that the small galaxies are more sensitive to the variation of PSF.

Moreover, we generate 3 different PSF models using TinyTim (Krist et al. 2011): the first one is a normal PSF without defocus, the second one is a bit larger but still realistic PSF, which is generated by changing the parameter defocus offset of secondary mirror to the primary, the third one is simply transposing of the first one. In Fig.9, we do not find significant effects with slight variations on the PSF. This may be because we used the circular symmetric, noise free images in the tests. For real galaxy noisy images, the PSF may cause slightly stronger effects. In additional tests, we calculate circular averages of the three PSF models, and find slightly different CG bias when using the second model PSF, since it has slightly larger size. Thus, the limited accuracy of the PSF model in HST data will not be an important source of error in our study.

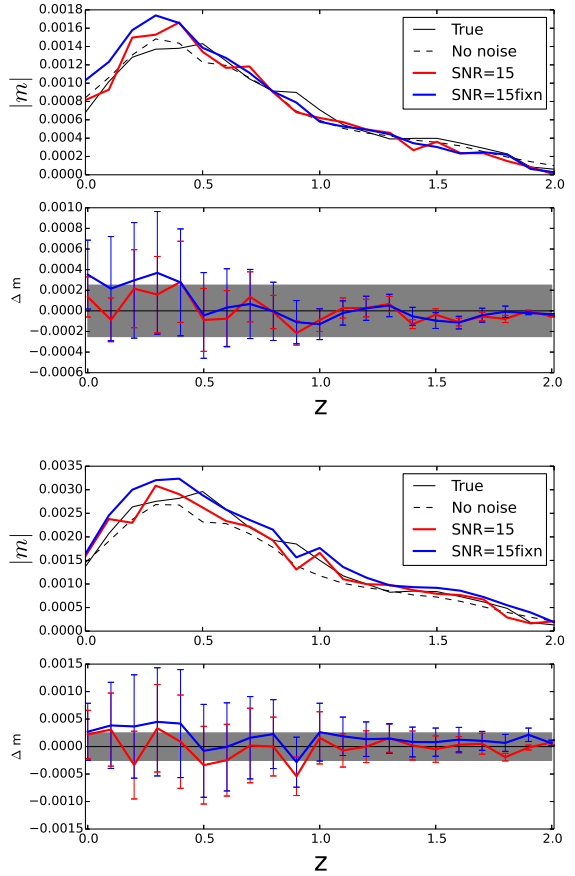


Figure 6. Same as Fig.5 but for images of $SNR = 15$. 200 realizations are used for the red lines at each redshift and 220(320) realizations are used for blues lines for the B-(S-)galaxy.

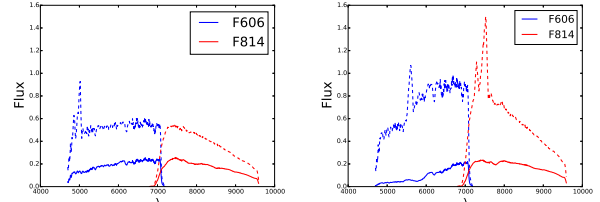


Figure 7. Spectral energy distributions used to create the disc and bulge components of our mock galaxies. They are normalized at $\lambda = 5500\text{\AA}$ by ratio $F_{\text{bulge}}/F_{\text{disk}} = 1/3$, and they are convolved with HST filter function in F606W and F814W. *left-* redshift 0; *right-* redshift 0.5.

4 CANDELS DATA

4.1 Calibration sample

In this section, we use the real galaxy images to estimate the CG bias which will appear in the Euclid weak lensing survey. For the reference PSF, we use the Airy model (Eq. 9).

To investigate the impact of colour gradients using realistic galaxies populations, we employ HST/ACS data taken in the F606W and F814W filters in the three CANDELS fields (AEGIS, COSMOS, and UDS), which have a roughly homogeneous coverage in both bands (see Davis et al. 2007; Grogin et al. 2011; Koekemoer et al. 2011). We base our analysis on a tile-wise re-

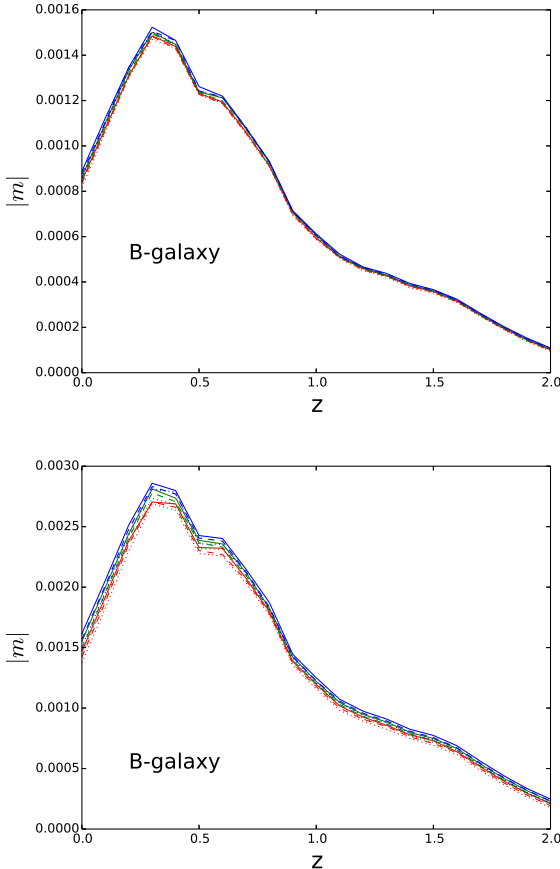


Figure 8. The PSF in the deconvolution are varied to see the effect on the CG bias. From red, green to blue lines, we increase the size of PSF for the F814W; from the solid, dashed to dotted lines we increase the size of PSF for the F606W.

duction of the ACS data, incorporating pointings which have at least four exposures to facilitate good cosmic ray removal, yielding combined exposure times of 1.3–2.3ks in F606W and 2.1–3.0ks in F814W. We employ the updated correction for charge-transfer inefficiency from Massey et al. (2014), MultiDrizzle (Koekemoer et al. 2003) for the cosmic ray removal and stacking, as well as careful shift refinement, optimised weighting, and masking for stars and image artefacts as detailed in Schrabback et al. (2010). Schrabback et al. (in prep.) describe the generation of weak lensing catalogues for these images. We base our analysis on the galaxies passing their source selection and apply additional magnitude cuts as detailed below. To investigate the dependence of the colour gradient influence on galaxy colour and redshift, we match this galaxy catalogue to the photometric redshift catalogue from Skelton et al. (2014). We list the total non-masked areas in which these catalogues overlap in Table 4.

We match the galaxy from V(F606W) and I(F814W) bands by selecting that the difference of galaxy coordinates in two bands is smaller than 1 pixel (0.05 arcsec). Moreover, in order to resemble the Euclid image survey, we apply selection based on the magnitude of two bands. In the first selection, the galaxy must be brighter than magnitude 25 in V-band and 24.5 in I-band. In the second selection (VIS, N2 sample), we apply the linear interpolation from V and I band using the effective wavelength to approximate the Euclid VIS magnitude, and select the galaxy brighter than 24.5 in

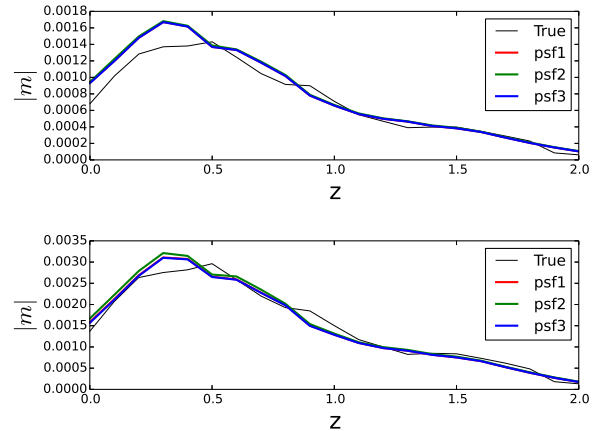


Figure 9. Same as Fig.8 but using three different TinyTim PSF model. Top (Bottom) is for the B-galaxy (S-galaxy).

Field	Area (arcmin ²)	N_1	N_2	N_3
AEGIS	180	2094	2112	3460
COSMOS	139	1593	1656	2449
UDS	146	1455	1497	2341
Total	465	5142	5265	8250

Table 4. Size of the HST CANDELS data sample in F606W and F814W bands. The number of galaxies are shown in three selection methods to match the Euclid survey, N_1 : $m_V < 25$ and $m_I < 24.5$, N_2 : $m_{VIS} < 24.5$, N_3 : $m_V < 25.5$ and $m_I < 25$.

VIS. In the last one (N3 sample), we enlarge the sample by using lower threshold in two bands: 25.5 in V and 25.0 in I band. The amount of galaxies is listed in Table 4. The galaxy VIS magnitudes will be determined by several factors, such as exposure time and filter transmission, etc. Thus, the actual number of galaxies can be different from what we have shown in this work. The approximation that we use rely on the flatness of the source spectrum. In the VIS sample, the number of galaxies is similar to that in the first selection in all three fields, which suggest that the spectra of our galaxies are relatively smooth. In the N3 sample the galaxy number is much higher. The total galaxy number and number density ($\sim 12/\text{arcmin}^2$) is lower than that in ES13 for several reasons: the galaxies are selected which the 3D-HST photometric redshift are available, and those suitable for weak lensing analysis, e.g. the very big or bright galaxies are not included. Moreover, in ES13 the galaxies are selected by the magnitude of F814W. However we select galaxies by the estimated VIS magnitude and well match in F606W and F814W.

There is no significant difference found in the distribution of galaxy parameters, such as effective radius, axis ratio, photometric redshift and colour (we use $m_{F606} - m_{F814}$ as colour in this work, and will write as m_{V-I} for short later). The SNR of most images in VIS sample are larger than 15, thus they will be able to provide relatively stable estimate for CG bias.

We also compare the galaxies from 3 catalogues (AEGIS, COSMOS, UDS). In the distribution of galaxy parameters (Fig. 10), we find no significant difference in half light radius (r_h), galaxy axis ratio or redshift distribution. However, in the colour distribution, there are more blue galaxies (small m_{V-I}) in AEGIS, which is more significant in N3 sample. We will see later that the colour of galaxy is also related to the CG bias in shape measurement.

4.2 CG bias from CANDELS

We estimate the CG bias following the same procedure for the simulated galaxy:

- fit the galaxy using one Sersic component for both band images. Some constraints such as Sersic index ($0.5 < n < 3.5$), effective radius ($1 < r_e < 50$ pixel) and axis ratio ($0.6 < q < 1.0$) are adopted in Galfit.
- interpolate the SED on each pixel of the galaxy image, and generate the galaxy at each wavelength (Eq.10 - 12), and then integrate over the wavelength to simulate the CG and NCG galaxy image.
- measure the shape of two images and calculate the bias m . We also apply 6 different orientation of the images in order to reduce the intrinsic shape noise.

In Fig.11, we show the histogram of the CG bias. The CG bias in most of the galaxies is smaller than 0.01 (94%). We did not perform averaging as we did for the simulated noisy images, which can further reduce the scatter of the bias. Thus the actual bias, especially the scatter in the sample, is smaller. In the bottom panel, we estimate the CG bias using a larger weight function ($2r_h$). As one expected, the bias decreases by about one order of magnitude.

Three PSF models from TinyTim, which are the same as in the previous section, are used in the deconvolution of CANDELS data. There is small difference among the three since the three PSF models have similar size. The following results are shown using the first PSF model from TinyTim.

In order to find a quick estimation for the CG bias, we try to find the relation between CG bias with galaxy parameters. In Fig.12, one can see the CG bias with the fitting parameters from two band images. On one side, we do not find any obvious relation between CG bias and ratio of Sersic index from two bands. On the other side, we see that there is an approximately linear relation between the ratio of effective radii and CG bias. Moreover, one expect that when $r_{e606} = r_{e814}$ and $n_{606} = n_{814}$, the CG bias in principle will be vanish, since the identical images from two bands will not have a colour gradient. In Fig.12, the blue lines are the binned average CG bias. In the bottom panel, one can see that the average bias meets zero at $r_{e814}/r_{e606} = 1$, as expected. However, in the Euclid VIS image survey, we will have only one band images, we thus need other methods for the bias estimation.

In Fig.11, the galaxies in AEGIS field have more positive CG bias than the galaxies in the other two. The colour distribution in AEGIS is different from the other two as well, which suggests the correlation between the CG bias and the colour of the galaxy. In Fig.13, we show the relation between the CG bias and the colour of the galaxies (here the colour is the magnitude different between V and I band). The bias is inversely proportional to the colour of the galaxies. The galaxy sample is split into two groups according to their colour: the red galaxies ($m_{V-I} > 0.5$) and the blue ones ($m_{V-I} < 0.5$). They are shown in the bottom panel of Fig.13 as a function of redshift. Most of the red galaxies are located at moderate redshifts, mainly between redshift [0.5, 1.0], while the blue galaxies are either at the lower redshift ($z < 0.5$) or higher redshift ($z > 1.0$). The CG bias in red galaxies are obviously more negative than that of the blue ones. The number density of very red galaxy ($m_{V-I} > 1$) is low and the scatters of the bias are large.

In Fig.14, we show the bias as a function of our mock VIS magnitude (m_{VIS}). There is no obvious dependence on m_{VIS} . Al-

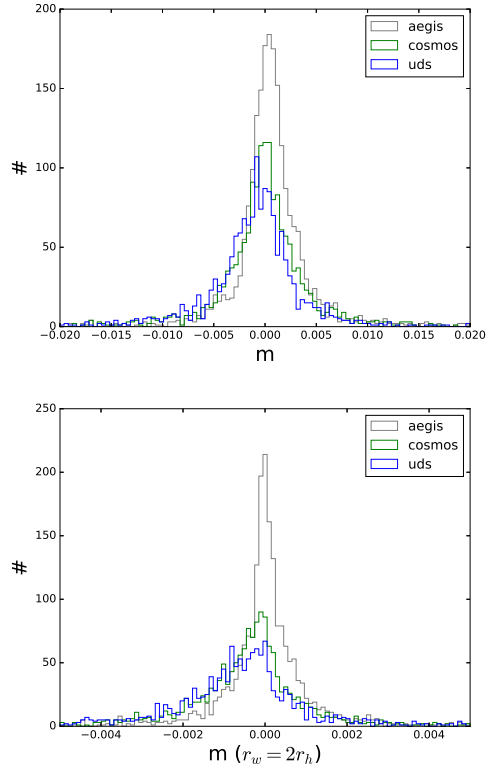


Figure 11. CG bias histogram from CANDELS: different colours show the result from three catalogues. In the bottom panel we show the CG bias using different weight function ($r_w = 2r_h$).

though the actual m_{VIS} is different from our linear approximation, also the filter transmission are different of two telescope, the correlation between m_{VIS} and CG bias will not be an accuracy method for CG bias.

Moreover, we stack the images from two bands as our mock VIS band images. Fig.15 shows the CG bias with the Sersic index and the effective radius fitted from the VIS images. In the top panel, we divide the sample into two groups by the fitted effective radius, either larger or smaller than 0.35 arcsec. The small (large) galaxies are shown by the blue (orange) points, and the blue (red) line is the bin average. The large galaxies cover a large range of Sersic index, have negative average CG bias. Most of small galaxies have small Sersic index (< 2.5). The bias of small galaxies are positive and approximately proportional to the Sersic index. The scatters of the bias for both large and small galaxies increase with the Sersic index. In the bottom panel, the galaxies are divided into three groups: the first is red galaxy whose color is large ($m_{V-I} > 1.0$); the second and third group are the rest galaxies either with large Sersic index ($n > 2.25$, elliptical galaxy) or small Sersic index (disk galaxy). The solid lines show the bin average over effective radius. We can see that the VIS image alone can also provide a rough estimation for CG bias, but classification of the galaxies is necessary. As shown in the figure, the disk galaxies have small bias, small radius (< 1 arcsec), and also small bias scatters. The elliptical galaxies cover large radius range, and the bias is larger than the disk ones. The bias in red galaxies are significant, and mainly negative. The scatters of red galaxies are larger than the other two kinds of galaxies. The multi-band photometry can definitely provide information on the CG bias, since the colour and

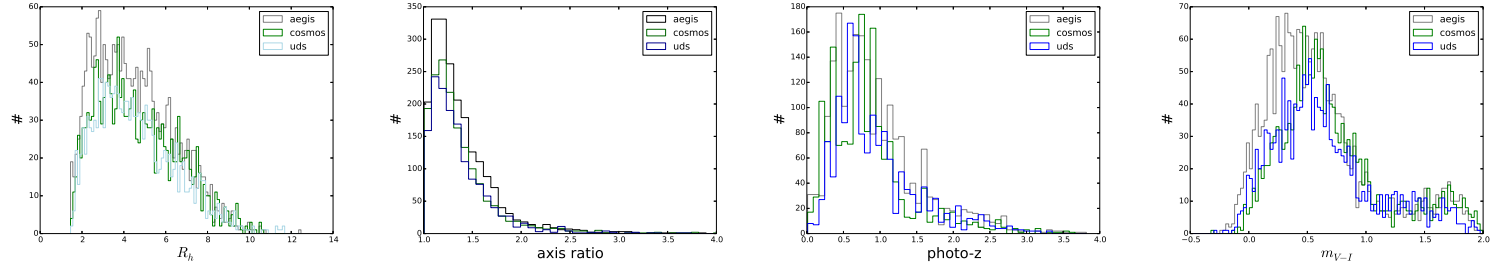


Figure 10. The histogram for basic galaxy properties in our sample. The lines with different colours represent galaxies from different catalogues (AEGIS, COSMOS, UDS). From left to right: half light radius, axis ratio, photometric redshift, and colour (m_{V-I}).

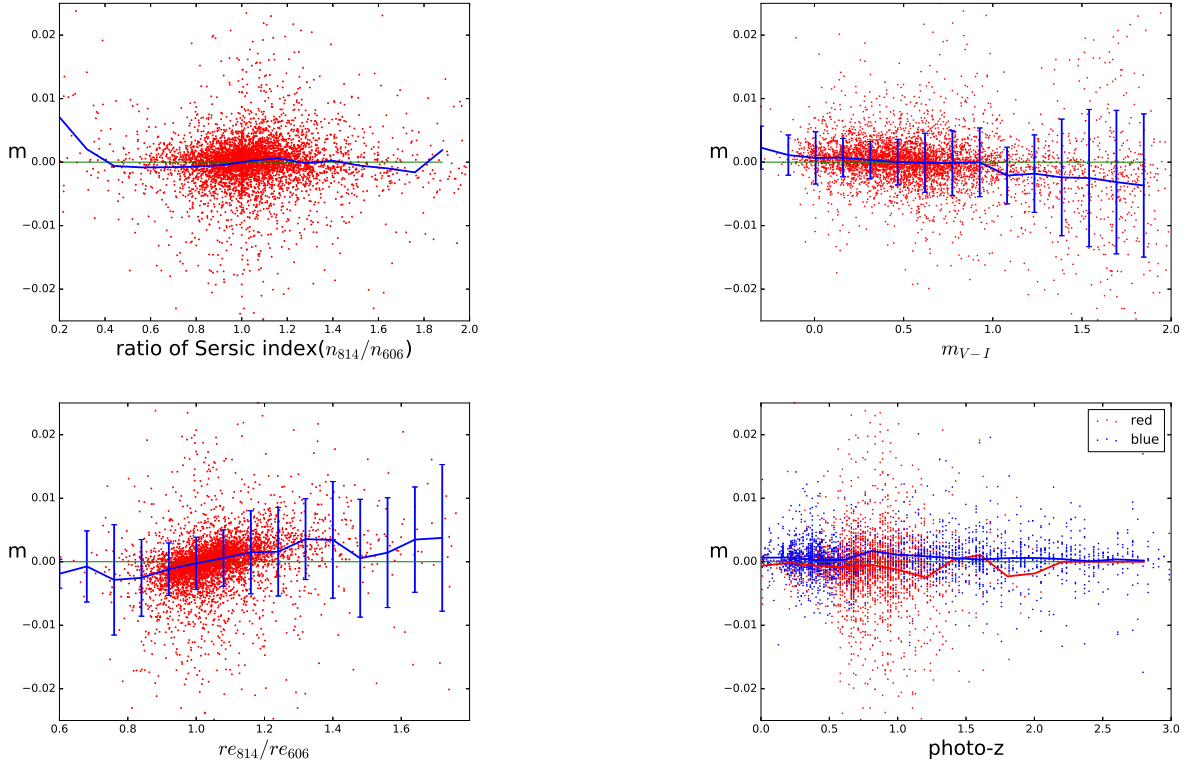


Figure 12. CG bias as a function of galaxy properties: ratio of Sersic index between two band (top) and effective radius between two bands (bottom). The blue lines are the average CG bias over the parameter bins.

colour gradient are correlated intrinsically during the evolution of galaxy. Moreover, the multi-band information is required for the photometric redshift study. One can obtain that for free to calibrate the CG bias. Although the dependence on the multi-band is different between photometric redshift and CG bias, the experience from photometric redshift can be used for CG bias, such as some machine learning algorithms.

We calculate the average bias and the dispersions over the redshift bins for both red ($m_{V-I} > 0.5$) and blue galaxies (Table 5). The red galaxies are mainly located between redshift (0.4, 1.2), while the blue galaxies are low density in redshift (0.8, 1.2). The bias from red galaxies are significantly smaller than that of blue galaxies, as one expected, the colour gradient in the elliptical galaxies are smaller. The dispersions of the bias in each bin are large, which probably indicate that in each bin there are several kinds and

Figure 13. CG bias as a function of galaxy properties, top: color (m_{V-I}), bottom: photo-z. In the bottom panel, the red and blue points are the bias for red ($m_{V-I} > 0.5$) and blue ($m_{V-I} < 0.5$) galaxies respectively. The lines are the average CG bias in the redshift bins.

sizes of galaxies. Therefore, in order to calibrate the bias with high precision, one need bigger galaxy samples. From our simulation, we need about 200 galaxies for one type of galaxy in every redshift bin. If we make rough bins, for instance, 2 types of colour: red and blue; 5 different sizes from about 0.1 arcsec to 1.0 arcsec (Fig.15), and 5 redshift bins, at least 10000 galaxies are required. For more realistic SED classifications and redshift bins, several times larger sample are also necessary.

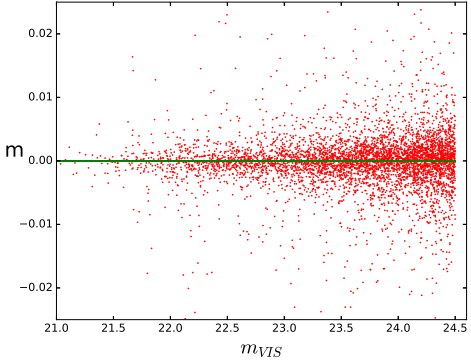


Figure 14. CG bias as a function of mock VIS magnitude.

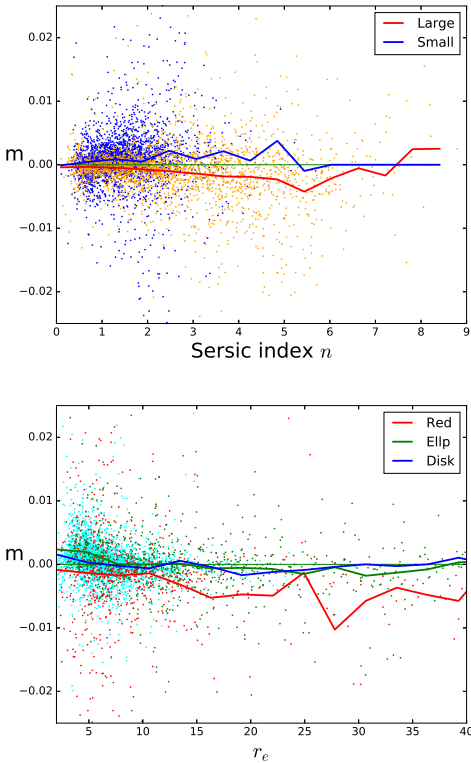


Figure 15. CG bias with Sersic index (top) and effective radius (bottom) from the mock VIS images. The unit of radius is a pixel ($= 0.05 \text{ arcsec}$). In the top panel, the blue (red) is the average of small (big) galaxies. In the bottom panel, the red line is average bias of red galaxy ($m_{V-I} > 1$); the green line is that of elliptical galaxy ($n_{\text{Sersic}} > 2.75$); the blue line is for the disk galaxy.

5 SUMMARY AND DISCUSSION

In the image survey for weak gravitational lensing, the wide band filter can provide high signal-to-noise images and large coverage of redshift range. There is however a shape bias due to the chromatic shape of galaxy and the PSF, which is named as colour gradient bias. For very wide band surveys, such as Euclid, this effect can cause a non-negligible bias. In this work, we exam such a kind of bias in measuring the shape of a galaxy using both simulated images and real data taken from the HST ACS CANDELS survey. In

photo-z	Number	\bar{m}	σ_m
0 – 0.4	187	-1.3×10^{-3}	0.012
0.4 – 0.8	1415	-7.6×10^{-4}	0.011
0.8 – 1.2	1116	-1.0×10^{-3}	0.017
> 1.2	245	-2.1×10^{-3}	0.015
0 – 0.4	667	6.6×10^{-4}	0.0026
0.4 – 0.8	513	2.8×10^{-4}	0.0028
0.8 – 1.2	187	1.2×10^{-3}	0.0041
> 1.2	935	5.4×10^{-4}	0.0046

Table 5. The number, average CG bias and dispersion in redshift bins for blue (bottom half) and red (top half) galaxies.

the simulated galaxy images, we confirm the bias behaviour from previous results (ES13). We further apply the calibration method to the noisy images in the simulations, and find that with reasonable signal-to-noise ratio (SNR = 15) and numbers of galaxies (300 images for one type of galaxy in one redshift bin), we can estimate the CG bias to a high precision. However, the underestimate cannot be avoided due to strong emission lines, or the uneven SED of source galaxies. Moreover, the SNR of the simulated images in two bands are assumed to be the same. In reality, the signal-to-noise in different bands are correlated to the SED of the galaxies.

We also apply the calibration method to the galaxy images taken by HST in two filters (F606W, F814W). In the estimation using CANDELS data, we find that most of the CG bias ($|m|$) is smaller than 0.01. As we find from simulated images, the estimation using noisy image has a large scatter, thus the CG bias in reality may be smaller than that shown here. In our sample of galaxies, the CG bias shows a correlation with the colour of galaxies, and a linear relation with the ratio of two band images. In case there is only one wide band image, one can also classify the galaxy by their Sersic index. The galaxies with small Sersic index, i.e. disk-like, have smaller CG bias. On the other hand, those with large Sersic index have large bias and also bias variation. Since the bias depends on the size of the galaxies as well, we can have an approximate fitting formula for the bias for different galaxy morphology. The fitting is limited to the galaxies in our sample, further investigation for different type of galaxies is necessary. The photometry from several bands, which will be used to estimate the redshift, can be also use for the CG bias analysis. Although the redshift dependence is not significant in our sample of galaxies, this may not be the case for a larger survey. In order to fully calibrate the bias for different redshift, a larger sample is essentially necessary. Moreover, in the weak lensing study, the colour of galaxies can be also used for the intrinsic alignment analysis. There is a potential correlation between the CG bias and the intrinsic alignment noise.

It has been shown that colour gradients depend on the environment where galaxies reside, with steeper colour gradients in poor rather than rich clusters (e.g. La Barbera et al. 2005), which is possible due to the different processes during galaxy formation. Close galaxy pairs or nearby bright star(s) will also cause brightness/colour gradient, which can affect our estimate for CG bias as well. The significance of the environment to CG bias is not clear and requires further study as well. Moreover, in the calibration we linearly interpolate the SED on pixels from two bands. Some advanced method to estimate the SED (e.g. Joseph et al. 2016) may help to improve the calibration of the bias.

In this work, we use the brightness moments to estimate the ellipticity of the galaxy. The PSF correction is not taken into account. The bias thus will appear in any method of measurement. However, the bias using the measurement method for real data will

be different, since every method has its own property and weight function. The CG bias will have method-dependent properties as well, although they will in principle have same dependence on the colour gradient of the galaxy images. As the first step of the CG bias analysis, we did not adopt any specific method in order to obtain general properties of the CG bias. Before the real analysis of Euclid data, one needs to study the bias with specific methods and simulated images with real properties in the Euclid weak lensing survey.

ACKNOWLEDGMENTS

We would like to thank Emiliano Merlin, Marco Castellano for helping on SExtractor and Galfit, Gary Bernstein, Adam Rogers, Junqiang Ge and also in general, the members of the Euclid Consortium for useful discussions. XE and VFC are funded by Italian Space Agency (ASI) through contract Euclid - IC (I/031/10/0) and acknowledge financial contribution from the agreement ASI/INAF/I/023/12/0. XE is also partly supported by NSFC Grant No. 11473032. JR is supported by JPL, which is run by Caltech under a contract for NASA, and is supported by grant NASA ROSES 12-EUCLID12- 0004. The fast Fourier transforms are supplied by the FFTW library (Frigo & Johnson 2005). We use CFITSIO (Pence 1999) for the FITS file.

APPENDIX A: RATIO OF MOMENT VS. PSF CONVOLUTION

In general, the PSF correction will cause extra bias in the shear estimation. In order to isolate the CG bias, we measure the brightness moments without applying any PSF correction methods in this work, i.e. the CG bias will appear in any method. Moreover, the definition of our CG bias uses the ratio of ellipticity from images, thus the estimate for the CG bias will not be changed by the convolution of a small PSF. Let us denote the quantity with prime for those convolved with PSF, i.e.,

$$I'(\theta) = \int d^2\psi I(\theta)P(\theta - \psi). \quad (\text{A1})$$

The weighted brightness moment can be written as

$$Q_{ij} = \int d^2\theta W(\theta) f_{ij}(\theta)I(\theta), \quad (\text{A2})$$

$$Q'_{ij} = \int d^2\theta W(\theta) f_{ij}(\theta) \int d^2\psi I(\psi)P(\theta - \psi), \quad (\text{A3})$$

where $f_{ij}(\theta)$ is the function to characterize the brightness moments, e.g. $f_{ij}(\theta) = \theta_i\theta_j$ for the second order moment. We can replace the variable ψ by $r = \theta - \psi$, and Taylor expand with respect to ψ . Then the moment becomes

$$\begin{aligned} Q'_{ij} &= \int d^2\theta W(\theta) f_{ij}(\theta) \int d^2r I(\theta - r)P(r) \\ &\approx \int d^2\theta W(\theta) f_{ij}(\theta) \int d^2r P(r) \left[I(\theta) - \frac{\partial I(\theta)}{\partial r}r \right], \\ &= Q_{ij} \int d^2r P(r) - \int d^2\theta W(\theta) f_{ij} \int d^2r P(r) \frac{\partial I}{\partial r}r. \end{aligned} \quad (\text{A4})$$

The integral of $P(r)$ in the first term independent of the image of the galaxy, and equals to unity for normalised PSF. In case of circular symmetric PSF or the asymmetry is small, the second term

can be neglect. $Q'_{ij} \approx pQ_{ij}$, where p is only determined by the size of PSF. Thus, for small PSF we have the approximation

$$\frac{Q_{ij}^{cg'}}{Q_{ij}^{neg'}} \approx \frac{Q_{ij}^{cg}}{Q_{ij}^{neg}}, \quad (\text{A5})$$

which means that the small circular PSF will not change the CG bias in our definition.

REFERENCES

- Bacon, D. J., Goldberg, D. M., Rowe, B. T. P., & Taylor, A. N. 2006, MNRAS, 365, 414
 Bartelmann, M. & Schneider, P. 2001, Phys. Rep., 340, 291
 Bertin, E. & Arnouts, S. 1996, A&AS, 117, 393
 Coleman, G. D., Wu, C.-C., & Weedman, D. W. 1980, ApJS, 43, 393
 Cropper, M., Hoekstra, H., Kitching, T., et al. 2013, MNRAS, 431, 3103
 Cypriano, E. S., Amara, A., Voigt, L. M., et al. 2010, MNRAS, 405, 494
 Davis, M., Guhathakurta, P., Konidaris, N. P., et al. 2007, ApJ, 660, L1
 den Brok, M., Peletier, R. F., Valentijn, E. A., et al. 2011, MNRAS, 414, 3052
 Frigo, M. & Johnson, S. G. 2005, Proceedings of the IEEE, 93, 216, special issue on “Program Generation, Optimization, and Platform Adaptation”
 Goldberg, D. M. & Natarajan, P. 2002, ApJ, 564, 65
 Gonzalez-Perez, V., Castander, F. J., & Kauffmann, G. 2011, MNRAS, 411, 1151
 Grogin, N. A., Kocevski, D. D., Faber, S. M., et al. 2011, ApJS, 197, 35
 Heymans, C., Van Waerbeke, L., Bacon, D., et al. 2006, MNRAS, 368, 1323
 Hoekstra, H., Franx, M., Kuijken, K., & Squires, G. 1998, ApJ, 504, 636
 Hoekstra, H. & Jain, B. 2008, Annual Review of Nuclear and Particle Science, 58, 99
 Joseph, R., Courbin, F., & Starck, J.-L. 2016, A&A, 589, A2
 Kaiser, N., Squires, G., & Broadhurst, T. 1995, ApJ, 449, 460
 Kennedy, R., Bamford, S. P., Häubler, B., et al. 2016, A&A, 593, A84
 Kitching, T. D., Miller, L., Heymans, C. E., van Waerbeke, L., & Heavens, A. F. 2008, MNRAS, 390, 149
 Koekemoer, A. M., Faber, S. M., Ferguson, H. C., et al. 2011, ApJS, 197, 36
 Koekemoer, A. M., Fruchter, A. S., Hook, R. N., & Hack, W. 2003, in HST Calibration Workshop : Hubble after the Installation of the ACS and the NICMOS Cooling System, ed. S. Arribas, A. Koekemoer, & B. Whitmore, 337
 Krist, J. E., Hook, R. N., & Stoehr, F. 2011, in Society of Photo-Optical Instrumentation Engineers (SPIE) Conference Series, Vol. 8127, Society of Photo-Optical Instrumentation Engineers (SPIE) Conference Series, 0
 La Barbera, F., De Carvalho, R. R., De La Rosa, I. G., et al. 2010, AJ, 140, 1528
 La Barbera, F., de Carvalho, R. R., Gal, R. R., et al. 2005, ApJ, 626, L19
 Laureijs, R., Amiaux, J., Arduini, S., et al. 2011, ArXiv: 1110.3193

- Massey, R., Hoekstra, H., Kitching, T., et al. 2013, MNRAS, 429, 661
- Massey, R., Schrabback, T., Cordes, O., et al. 2014, MNRAS, 439, 887
- Melchior, P., Viola, M., Schäfer, B. M., & Bartelmann, M. 2011, MNRAS, 412, 1552
- Meyers, J. E. & Burchat, P. R. 2015, ApJ, 807, 182
- Miller, L., Heymans, C., Kitching, T. D., et al. 2013, MNRAS, 429, 2858
- Miller, L., Kitching, T. D., Heymans, C., Heavens, A. F., & van Waerbeke, L. 2007, MNRAS, 382, 315
- Nakajima, R. & Bernstein, G. 2007, AJ, 133, 1763
- Pence, W. 1999, in Astronomical Society of the Pacific Conference Series, Vol. 172, Astronomical Data Analysis Software and Systems VIII, ed. D. M. Mehringer, R. L. Plante, & D. A. Roberts, 487
- Peng, C. Y., Ho, L. C., Impey, C. D., & Rix, H.-W. 2010, AJ, 139, 2097
- Rowe, B. T. P., Jarvis, M., Mandelbaum, R., et al. 2015, Astronomy and Computing, 10, 121
- Schrabback, T., Hartlap, J., Joachimi, B., et al. 2010, A&A, 516, A63
- Sembolini, E., Hoekstra, H., Huang, Z., et al. 2013, MNRAS, 432, 2385
- Skelton, R. E., Whitaker, K. E., Momcheva, I. G., et al. 2014, ApJS, 214, 24
- Tortora, C., Napolitano, N. R., Cardone, V. F., et al. 2010, MNRAS, 407, 144
- Voigt, L. M., Bridle, S. L., Amara, A., et al. 2012, MNRAS, 421, 1385